Microporous and Mesoporous Materials 324 (2021) 111298

Contents lists available at ScienceDirect

Microporous and Mesoporous Materials

journal homepage: www.elsevier.com/locate/micromeso

Steam-assisted synthesis of SAPO-34@ZSM-5 core-shell zeolite for enhancing the synergies of n-hexane-Methanol Co-Reaction to light olefins

Qitong Cheng [a], Benxian Shen [a,b,*], Jichang Liu [a,b,**], Hui Sun [a,b], Di Wu [c], Lei Jiang [a], Peikun Yan [a], Xin Pu [a], Suhui Ou [a], Jigang Zhao [a,b]

[a] State Key Laboratory of Chemical Engineering, School of Chemical Engineering, East China University of Science and Technology, Shanghai, 200237, China
[b] International Joint Research Center of Green Energy Chemical Engineering, East China University of Science and Technology, Shanghai, 200237, China
[c] Department of Chemistry, Washington State University, Pullman, WA, 99163, USA

ARTICLE INFO

Keywords:
Core-shell configuration
Steam-assisted synthesis
Co-reaction
Composite zeolites
Light olefins

ABSTRACT

An alternative and promising route for the production of light olefins which realizes the objective of effective resource usage is the coupling conversion of *n*-hexane-methanol. The SAPO-34@ZSM-5 core-shell composite has been designed and fabricated by the steam-assisted crystallization (SAC) method for boosting the *n*-hexane-methanol synergies. SAC avoids the undesired phase transformation/dissolution of SAPO-34 caused by exposure to harsh basic conditions of the ZSM-5 precursor solution. In comparison with the nanosized ZSM-5 or physical mixture, the SAPO-34@ZSM-5 core-shell zeolite demonstrates a 32–38 wt% increase in the light olefin selectivity, a 28–67 wt% increase in the *n*-hexane conversion, and an 89–143% improvement in the catalyst lifetime under identical reaction conditions. With the aid of GC-MS analysis of carbonaceous deposits in spent catalysts, higher polymethylbenzenes concentration and lower polycyclic aromatic hydrocarbon (PHA) concentration are obtained from the extracted species of spent SAPO-34@ZSM-5 in comparison with that of other samples, which suggests the aromatic-based route to light olefins is enhanced and the carbonaceous deposition is slowed down. The core-shell configuration of the SAPO-34@ZSM-5 composite diminishes the diffusion rate of methanol towards the SAPO-34 core layer and increases the coupling of *n*-hexane derivatives with methanol in the hydrocarbon pool (HCP) route. The decreased number of acidic sites on the external surface of the SAPO-34 core layer may also be accounted for the inhibited carbon deposition.

1. Introduction

As vital constituents in the modern petrochemical industry, ethylene and propene have been broadly used for the production of an entire range of key intermediate chemicals, including polymers and oxygenates. Conventionally, light olefins are produced through steam pyrolysis of naphtha, which is subject to energy-extensive consumption, insufficient light olefin selectivity, and an inflexible product slate [1,2].

Given the energy balance and efficient use of petroleum resources, the jointed reaction of the exothermic methanol to olefin (MTO) reaction and endothermic hydrocarbons cracking is first proposed by Lücke et al. [3]. The coupled transformation of methanol with C4 hydrocarbon, liquid hydrocarbon, and crude naphtha participation between 600 and 700 °C was investigated for higher light olefin yields. Meanwhile, the mechanism of the coupling reaction between methanol and hydrocarbons has been studied and discussed [4–8]. Kazemi et al. [5] investigated the effects of the addition of C5/C6 and C4 hydrocarbons to the methanol to propylene reaction and found that propene selectivity in the process was enhanced significantly at moderate temperatures (470–500 °C). The integration of the C4–C6 hydrocarbon byproducts into the dual cycle mechanism of MTO was found. As illustrated in Fig. 1, the MTO reaction on acid zeolite catalysts is dominated by an efficient indirect hydrocarbon pool (HCP) route, including aromatic-based cycle and alkene-based cycle routes [9–14]. The initial alkene can be formed by the methanol conversion in the induction period [15], which is the active intermediates in the alkene-based cycle, and simultaneously,

* Corresponding author. State Key Laboratory of Chemical Engineering, School of Chemical Engineering, East China University of Science and Technology, Shanghai, 200237, China.
** Corresponding author. State Key Laboratory of Chemical Engineering, School of Chemical Engineering, East China University of Science and Technology, Shanghai, 200237, China.
E-mail addresses: sbx@ecust.edu.cn (B. Shen), liujc@ecust.edu.cn (J. Liu).

https://doi.org/10.1016/j.micromeso.2021.111298
Received 8 May 2021; Received in revised form 24 June 2021; Accepted 8 July 2021
Available online 16 July 2021

alkenes can convert to methylbenzene by the oligomerization and cyclization reactions (black line in Fig. 1). Alkenes and poly-methylbenzene carbocation, as the active intermediates, are decisive for light olefins selectivity. In the alkene-based cycle, propylene and heavier than propylene are produced by the continuous methylation cracking of alkenes (red line in Fig. 1). In the aromatic-based cycle, poly-methylbenzene is repeatedly methylated and dealkylated to form light olefins (blue line in Fig. 1). Based on the previous reports, xylene and tri-methylbenzene act as the key contributors for ethylene increase, as well as heavier methylbenzenes (involving in tetra-methylbenzene, penta-methylbenzene and hexa-methylbenzene) are decisive for propylene increase, which is attributed to the transition-state shape selectivity [12]. In addition, the length of the diffusion path is also one of the factors affecting the selectivity of ethylene and propylene [16]. For hydrocarbons pyrolysis over zeolite catalysts, the mechanism of the carbocation is followed [17,18]. Cordero-Lanzac et al. [4] explored the synergies during combined reactions of *n*-pentane with methanol/dimethyl ether. A bidirectional promotion effect was found when the coexistence of the two well-established mechanisms on the ZSM-5 zeolite.

Some work has been performed in this field of coupled conversion of methanol-hydrocarbon, focused on reaction conditions and the mechanisms of coupled reactions [20–22]. There are few studies on catalysts aimed at enhancing the synergy in the combined reactions of hydrocarbon with methanol. ZSM-5 zeolite is the most broadly studied catalyst for combined reactions of hydrocarbon with methanol due to its unique porosity and acidity [23–25]. The strong acid properties and straight pores of ZSM-5 not only promote the cracking of hydrocarbon [26], and could also allow MTO to proceed through a dual cyclic route (involving alkene-based route and aromatic-based route). Noteworthily, the aromatic-based route in ZSM-5 is limited because the pore structure of ZSM-5 cannot provide enough spaces for the formation of the heavy methylbenzenes, as the high active species in aromatic-based route for MTO conversion [27]. For the aromatic-based route of MTO, SAPO-34 exhibits excellent performance because its large pore cage provides a superior reaction domain for the aromatic-based route and its narrow pore mouth presents a high selectivity for light olefins [28,29]. While the rapid inactivation of SAPO-34 is the main factor hindering its wide application. The individual pore structure and acid properties of conventional zeolites limit their contribution to the combined reactions [29]. Based on the above results, the preparation of SAPO-34@ZSM-5 core-shell zeolite is necessary for strengthening the synergies of the hydrocarbons catalytic cracking into the HCP route of MTO.

ZSM-5(core)/SAPO-34(shell) binary composite zeolites were synthesized via the hydrothermal crystallization of SAPO-34 on the surface of ZSM-5 crystals and utilized for various catalytic reactions [30–32]. Chae et al. [33] conducted a comparative study of MTO over ZSM-5/SAPO-34 binary composite zeolites that were synthesized by seed synthetic method, series synthetic method and physical mixture, respectively. The result suggested that the synergistic effect between ZSM-5 and SAPO-34 tuned the physicochemical and catalytic properties of composite zeolites during the synthesis process. Moradiyan and co-workers [34] focused on nanocomposite ZSM-5(core)/SAPO-34 (shell) developed by one-step ultrasound-assisted hydrothermal crystallization in which ZSM-5 power was mixed with SAPO-34 synthetic gel and irradiated with ultrasound at a frequency of 24 kHz. Their results displayed that the ultrasonic-assisted crystallization enabled shorter synthesis time, smaller crystallite size, higher specific surface area and more mesoporous structure. Rownaghi et al. [35] employed an additive manufacturing method for preparation 3D-HZSM5 and then used a hydrothermal SAPO-34 crystallization to obtain 3DHZSM5@SAPO-34 composite with SAPO-34 grown on the surface of each HZSM-5 structured monoliths, which enhanced the density of strong acid sites and caused further conversion of DME to higher hydrocarbons.

The above described ZSM-5/SAPO-34 binary composite zeolites are normally constructed by the second crystallization of the mixture of ZSM-5 crystals and SAPO-34 precursor gel. However, in regard to the preparation and application of SAPO-34(core)/ZSM-5 (shell), there are limited reports as a result of the instability of SAPO-34 zeolite crystals in ZSM-5 strong basic precursor gel. SAPO-34 zeolite with low framework density is easily dissolved in ZSM-5 highly basic precursor gel which alters the chemical composition of shell precursor gel and the morphology of core phase, so far as to affect the secondary crystallization. The dissolution of SAPO-34 crystals as the core phase in the ZSM-5 highly basic precursor gel is a major obstacle for preparing the SAPO-34 (core)/ZSM-5 (shell) composite materials. Besides, the hydrophobicity of SAPO-34 particles is isolated from the aluminosilicate field, which difficultly builds a perfect core-shell structure [36]. Razavian et al. [37] successfully fabricated SAPO-34(core)/ZSM-5(shell) composite by an efficient pretreatment procedure to coat SAPO-34 crystals with tetrapropyl ammonium cations (TPA^+), additionally, the pre-crystallization process of ZSM-5 also diminished the alkalinity of the mixture. However, for the well-defined SAPO-34(core)/ZSM-5(shell) zeolite, the crystallization conditions in hydrothermal synthesis are still stringent.

At present, the steam-assisted crystallization (SAC) method has been applied in the synthesis of single-phase zeolites because of its high yields and simplicity [38–40]. In this paper, the SAPO-34@ZSM-5 core-shell zeolite composite is firstly synthesized by the SAC method of ZSM-5 dry gels mixed with TPA-SAPO-34 powder and used to enhance the synergistic conversion of *n*-hexane-methanol to light olefins. This method takes full advantage of water-incompatible SAPO-34 in synthesizing binary-phase SAPO-34@ZSM-5 core-shell zeolite composites.

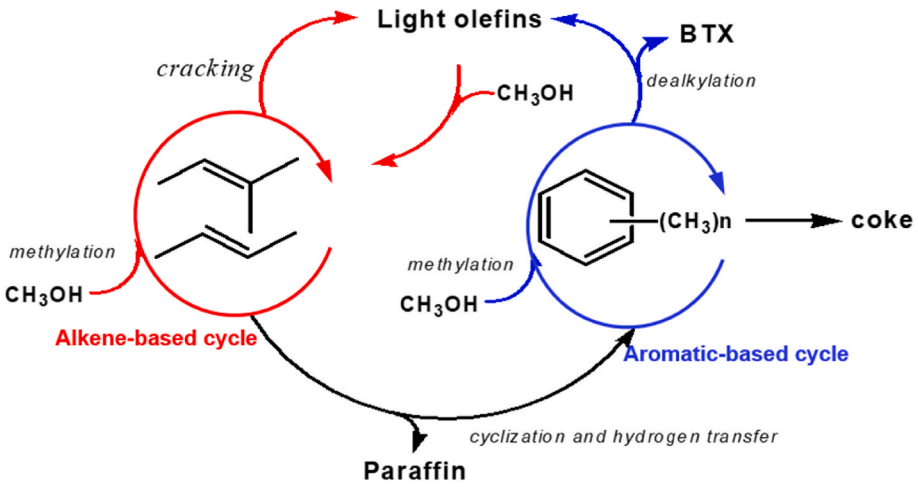

Fig. 1. The simplified schemes of the HCP mechanism [14,19].

Accordingly, the dissolution and collapse of the SAPO-34 structure in the harsh basic precursor gel of ZSM-5 are avoided. The catalytic performance and speciation of the trapped organic species over the SAPO-34@ZSM-5 core-shell zeolite composite were studied in detail and compared with those of pure ZSM-5 and SAPO-34 and their physical mixture. Based on the obtained results, the effect of the core-shell configuration of the composite on the reaction routes of coupled *n*-hexane and methanol was investigated and discussed.

2. Experimental section

2.1. Materials and reagents

n-Hexane (AR, Sinopharm Chemical Reagent Co., Ltd.), methanol (AR, Sinopharm Chemical Reagent Co., Ltd.), aluminum isopropoxide (Al(OPri)3, 99.0 wt%, Macklin Biochemical Co., Ltd.), tetraethyl orthosilicate (TEOS, 28.4 wt% SiO_2, Sinopharm Chemical Reagent Co., Ltd.), tetrapropylammonium hydroxide (TPAOH, 40.0 wt % in water, Aladdin Biochemical Technology Co., Ltd.), sodium hydroxide (NaOH, 98 wt%, Titan Chemical Co., Ltd.), ammonium chloride (NH_4Cl, AR, Aladdin Biochemical Technology Co., Ltd.), pseudoboehmite (PB, AR, Macklin Biochemical Co., Ltd.), triethylamine (TEA, GC, Aladdin Biochemical Technology Co., Ltd.), orthophosphoric acid (H_3PO_4, 85 wt %, Macklin Biochemical Co., Ltd.), colloidal silica (30.0 wt% SiO_2, Macklin Biochemical Co., Ltd.), tetrapropylammonium bromide (TPABr, 98.0 wt%, 3A Chemical Co., Ltd.), and propanol (99.5 wt%, 3A Chemical Co., Ltd.) were utilized.

2.2. Synthesis procedures

2.2.1. ZSM-5

The ZSM-5 was fabricated by a SAC method with a molar composition of 1.25 Al_2O_3: 100.0 SiO_2: 0.4 Na_2O: 24.0 TPAOH: 1920.0H_2O: 400.0 ethanol (EtOH). First, TEOS was instilled into a mixed solution of NaOH, TPAOH, and DI water, followed by continuous stirring in a Teflon beaker for 10 h at 298 K to form a homogenous solution. Then, $Al(OPri)_3$ was dissolved in the homogenous solution slowly under agitation for 24 h at 298 K before dispersing in a dish for solvent evaporation under reduced pressure. The as-prepared dry gel was moved into a 10-mL Teflon beaker and then transferred to a 100-mL Teflon-lined autoclave filled with DI water ($m_{\text{dry gel}}$: $m_{\text{distilled water}}$ = 1:3) at the bottom of the autoclave. This autoclave was heated at 135 °C for 84 h. The solid product was washed with ID water, air-dried overnight, and finally calcined in air at 550 °C for 5 h. The calcined sample was modified by ion exchange with 1 M NH_4Cl solution, followed by calcination again in the air at 550 °C for 3 h to form an H-form zeolite, denoted as ZSM-5.

2.3. SAPO-34

The SAPO-34 sample was synthesized with a molar composition of 1.0 Al_2O_3: 1.0 P_2O_5: 0.6 SiO_2: 2.0 TEA: 0.2 TEAOH: 60.0H_2O. H_3PO_4 was diluted with DI water with vigorous stirring, and PB was added stepwise and dissolved completely. Colloidal silica was instilled into the above solution and stirred for 2 h to form a homogenous solution. TEAOH and TEA were then dropped in the homogenous solution and stirred for another 6 h to form the precursor gel. The precursor gel was moved into a 100-mL Teflon-lined stainless steel autoclave for 24 h of aging and crystallized hydrothermally at 200 °C for 24 h. The product was obtained by centrifugation, washed with DI water, and finally calcined in air at 550 °C for 5 h. The synthesized sample was labeled SAPO-34.

2.3.1. SAPO-34@ZSM-5 core-shell zeolite composite

The SAPO-34@ZSM-5 core-shell zeolite composite was fabricated by SAC of ZSM-5 as-prepared dry gel and TPA-SAPO-34 powder. SAPO-34 was coated by ion exchange with 1 M TPABr propanolic liquor at 333 K and then filtered and dried at 100 °C for 12 h. The product was labeled TPA-SAPO-34. The as-prepared ZSM-5 dry gel was produced according to the method described in Section 2.2.1. Then, the TPA-SAPO-34 crystals were added to the ZSM-5 dry gel ($m_{\text{TPA-SAPO-34 crystals}}$: $m_{\text{ZSM-5 dry gel}}$ = 0.3:1) under sustained mixing and ground to form a well-mixed white powder. The well-mixed white powder was moved into a 10-mL Teflon beaker and then transferred to a 100-mL Teflon-lined autoclave with DI water at the bottom of the autoclave ($m_{\text{white power}}$: $m_{\text{distilled water}}$ = 1:3). This autoclave was heated at 135 °C for 84 h. The solid product was washed with DI water, air-dried overnight, and finally calcined in air at 550 °C for 5 h. The calcined sample was modified by ion exchange with 1 M NH_4Cl solution, followed by calcination again in the air at 550 °C for 3 h to form a zeolite composite marked as SAPO-34@ZSM-5. The SAPO-34@ZSM-5 is abbreviated to S34@Z5 in the following text. Accordingly, S34@Z5 samples are synthesized by SAC, and the procedure is given in Fig. 2.

2.3.2. Physical mixture

The ZSM-5 synthesized by the method described in Section 2.2.1 and the SAPO-34 synthesized by the method described in Section 2.2.2 ($m_{\text{TPA-SAPO-34 crystals}}$: $m_{\text{ZSM-5 dry gel}}$ = 0.3:1) were blended by adequate grinding in an agate mortar to produce physical mixtures labeled PMS34/Z5.

2.3.3. Hydrothermal synthesis of samples

To prepare the SAPO-34@ZSM-5 by a conventional hydrothermal method crystallization of ZSM-5 precursor gel and TPA-SAPO-34 powder. The TPA-SAPO-34 powders were added to the as-prepared ZSM-5 precursor gel under sustaining agitation to form a well-mixed solution. The solution was then transferred to a 100 mL Teflon-lined autoclave and using identical crystallization conditions. The calcined sample was modified by ion exchange with 1 M NH_4Cl solution, followed by calcination again in the air at 550 °C for 3 h to form an H-form zeolite abbreviated as S34/Z5(HY).

2.4. Catalyst characterizations

X-ray diffraction (XRD) patterns were recorded using a Bruker D8 Advance X-ray diffractometer (Bruker AXS Inc., Germany) operated at 40 kV and 40 mA with Cu Kα monochromatized radiation (λ = 1.5418 Å). The samples were scanned from 5 to 50° at a rate of 5.0°/min. The crystal morphology images of the samples were recorded using a Nova NanoSEM 450 instrument. The elemental compositions were characterized by Falcon energy-dispersive spectrometry (EDS) (EDAX Inc., USA). The structure of the catalysts was evaluated with high-resolution transmission electron microscopy (HRTEM) with a JEM-2100 electron microscope at 200 kV (JEOL Co., Ltd., Tokyo, Japan). Textural properties, including specific surface areas, micropore volume, and total pore volume, were determined using an ASAP 2020 automatic physisorption analyzer (Micromeretics, Norcross, US) and calculated by Brunauer-Emmett-Teller (BET), t-plot, and nonlocalized density functional theory (NLDFT) methods, respectively. NH_3 temperature-programmed desorption (NH_3-TPD) was performed on an AutoChem 2020 automatic temperature-programmed desorption instrument (Micromeritics, Norcross, US). Thermogravimetric analysis (TGA) was conducted on a PerkinElmer Diamond TGA apparatus to determine the total coke content. The experiment was conducted with 10 mg spent zeolite, under 80 mL/min air flowing, and the ramp rate was 10 °C/min.

2.5. Carbonaceous deposits analysis

The organic components were liberated from 0.4 g of spent zeolite by the dissolution of the aluminosilicate matrix in 2 mL of 40% hydrofluoric acid solution, followed by the extraction of soluble organic components using 4 mL of CH_2Cl_2 as the solvent. The soluble organic components were then neutralized using 2 mL of 0.5 M sodium carbonate solution. Finally, the soluble organic components were analyzed

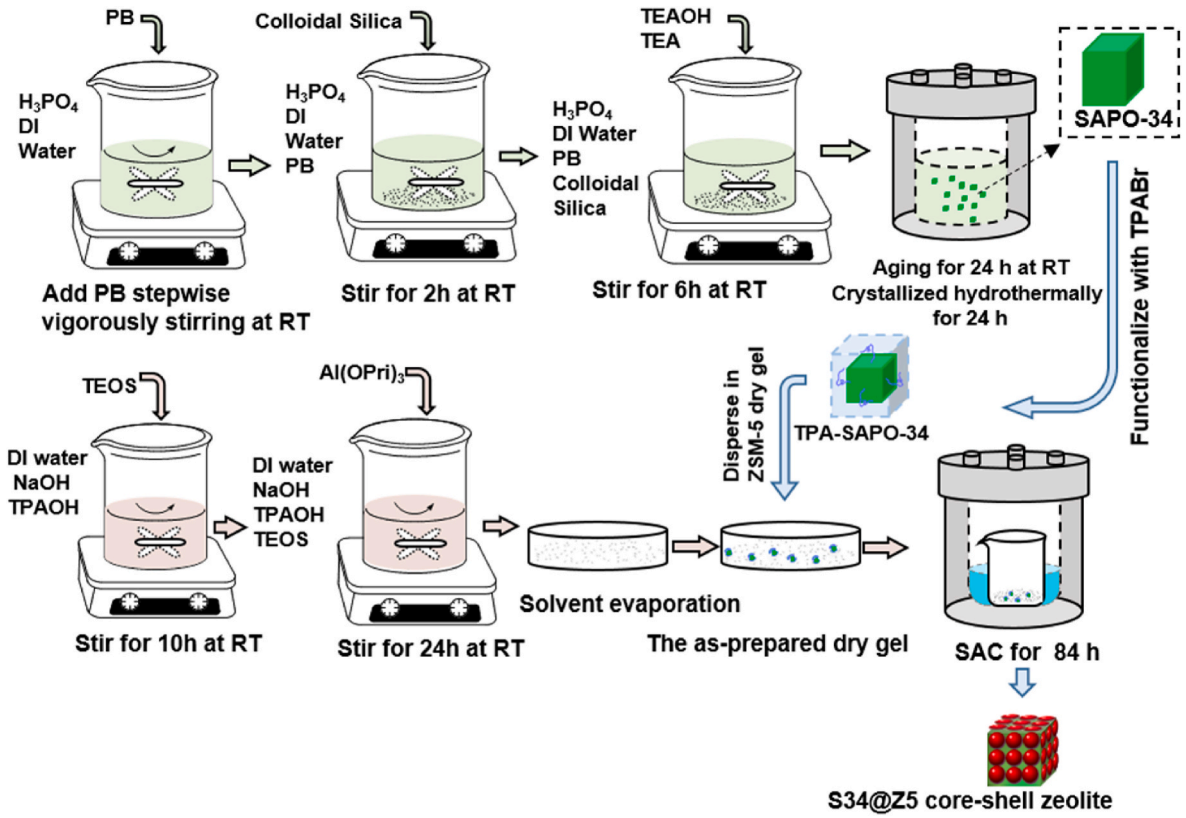

Fig. 2. Schematic for the steam-assisted synthesis of S34@Z5 core-shell zeolite composite.

by using GC-MS.

2.6. Catalysis test

The catalytic performance of the as-prepared zeolite catalysts for the coupling reaction of *n*-hexane and methanol was investigated at atmospheric pressure in a fixed-bed reactor (Fig. 3). The weight hourly space velocity (WHSV) for the test was 10 h^{-1}. The catalyst (40–60 mesh) was pretreated at 600 °C in a 30 mL/min flow of N_2 for 1 h and then cooled to 580 °C for reaction. *n*-Hexane and methanol were pumped at a molar ratio of 1.0:1.6 from the top of the fixed-bed reactor, and a 30 mL/min flow of N_2 to the reactor was controlled by a mass flow controller. The gas products involved in hydrocarbons and nonhydrocarbons were analyzed by gas chromatography (Shimadzu GC-2014, equipped with an FID detector, Plot/Al_2O_3 capillary column, TCD detector, and 13X packed column). The liquid products were analyzed by gas chromatography (Shimadzu GC-2010, equipped with an FID detector and Rtx-1 PONA capillary column).

The *n*-hexane conversion, Cn, is as follows:

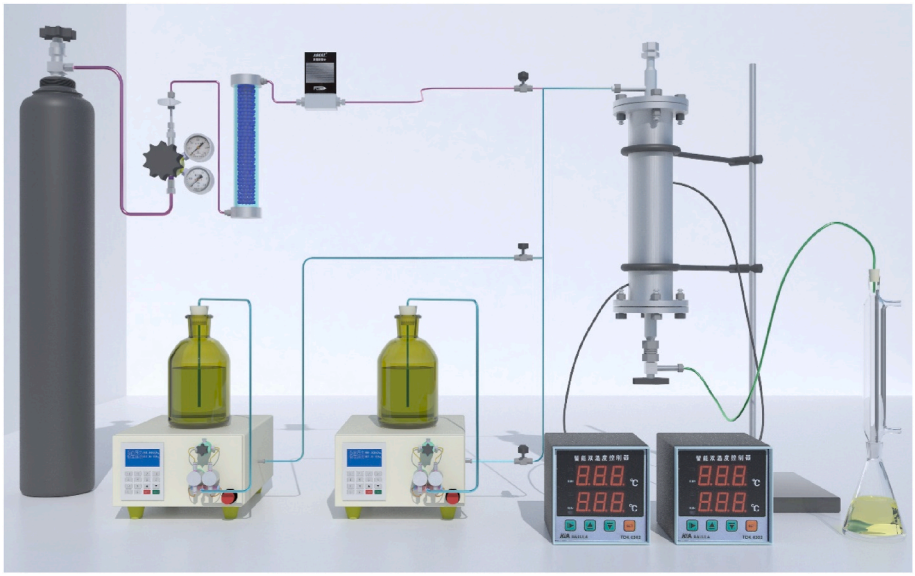

Fig. 3. Experimental setup for catalytic performance evaluation.

$$C_n = 100 \times \frac{m_{nin} - m_{nout}}{m_{nin}}$$

m_{nin} and m_{nout} are the masses of *n*-hexane in raw materials from the inlet and outlet of the reactor, respectively.

The methanol conversion, *Cm*, is as follows:

$$C_m = 100 \times \frac{m_{min} - m_{mout}}{m_{min}}$$

m_{min} and m_{mout} are the masses of methanol in raw materials from the inlet and outlet of the reactor, respectively.

The yield of organic product i is defined as follows:

$$Y_i = 100 \times \frac{m_i}{\frac{14}{32}m_{min} + m_{nin}}$$

m_i is the mass of organic product i at the outlet of the reactor, $\frac{14}{32}m_{min}$ is defined as the mass of the organic component in methanol from the inlet of the reactor.

3. Results and discussion

3.1. Catalysts characterization

The XRD patterns of the ZSM-5, SAPO-34, physical mixture PMS34/Z5, S34@Z5 (HY), and S34@Z5 core-shell composite are presented in Fig. 4. The peaks at 2θ = 7.9, 8.8 and 23.1 ascribed to ZSM-5, as well as the peaks at 9.5, 12.9, 16.0 and 20.5 belonging to SAPO-34, can be obtained from the XRD patterns of ZSM-5 and SAPO-34, indicating that ZSM-5 and the SAPO-34 zeolite are successfully manufactured through SAC and severe hydrothermal crystallization. The absence of the SAPO-34 diffraction peak and the extremely low intensity of the ZSM-5 diffraction peak are obtained from the XRD patterns of S34/Z5 (HY) synthesized by hydrothermal synthesis. The characteristic peaks at 2θ = 7.9, 8.8 and 23.1 vested to ZSM-5 and those at 2θ = 9.5 and 12.9 vested

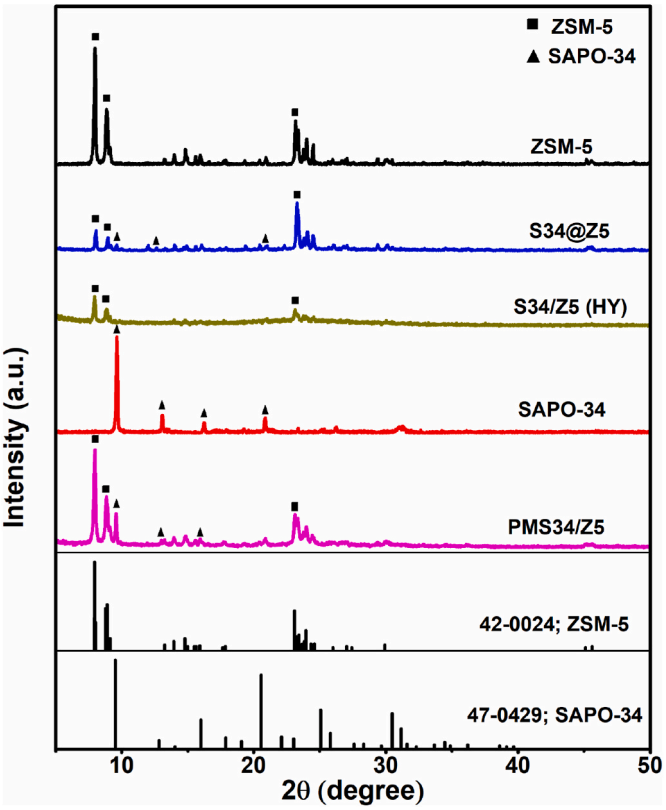

Fig. 4. XRD patterns of ZSM-5, S34@Z5, S34/Z5 (HY), SAPO-34 and PMS34/Z5.

to SAPO-34 can be observed in the XRD pattern of the steam-assisted synthesis S34@Z5 composite, although some characteristic peaks attributed to individual SAPO-34 phases overlap with ZSM-5, demonstrating that a binary structure is present in the obtained composite. The CHA structural pattern intensities of the S34@Z5 composite are small relative to that of PMS34/Z5, which could be caused by the growth of ZSM-5 on the surface of pretreated SAPO-34. Moreover, for the S34@Z5 composites, the peak intensities at 2θ = 7.9 and 8.8° corresponding to the (101) and (200) planes of ZSM-5 became small in comparison to those of the as-prepared single ZSM-5 and physical mixtures, while the peak intensities at 2θ = 23.1 and 23.9° corresponding to the (501) and (303) planes barely changed. It seems that SAPO-34 was partly dissolved or that the interfacial interaction between ZSM-5 and SAPO-34 occurred on specific crystal surfaces in the crystallization process of ZSM-5.

The SEM images of the ZSM-5, SAPO-34, S34@Z5 core-shell zeolite composite, and S34/Z5(HY) are presented in Fig. 5A. The spherical structure is observed for ZSM-5 nanoparticles with a uniform size of ca. 150 nm. The SAPO-34 particles exhibit a uniform cubic structure with a size of ca. 2 μm. For the S34@Z5 core-shell composite, the SEM image attests to the overgrowth of ZSM-5 spheroidal nanocrystals on the surface of pretreated SAPO-34 with good core-shell morphology, despite the shell layer formed by ZSM-5 particles being unevenly coated on the surface of SAPO-34. The incomplete crystallization of ZSM-5 and the disappearance of SAPO-34 are observed from the SEM image of S34/Z5 (HY), which could be related to the dissolution of SAPO-34 in the ZSM-5 alkaline precursor gel. The elemental mappings of the S34/Z5 (HY) in Fig. 5B support the above inference, in which large amounts of P and small amounts of Al are dispersed in the nonmaterial region. Combined with the XRD and SEM characterization results of S34/Z5 (HY), the dissolution of SAPO-34 in the ZSM-5 alkaline precursor gel slows down the crystallization of ZSM-5 [41].

Fig. 6A displays the HRTEM micrographs of the as-prepared ZSM-5, SAPO-34, and S34@Z5. In the HRTEM image of ZSM-5, a spheroidal nanocrystal aggregate is observed, which is consistent with the SEM results (Fig. 5A). Additionally, there is a certain degree of orientation between adjacent nanoparticles, suggesting that they might be intergrown. Clearly, the TEM micrograph of SAPO-34 shows a typical rhombic single crystal. Fig. 6A (i)-(v) displays TEM images of the S34@Z5. Across-section is observed from Fig. 6A (ii), and the white slit is believed to be the micro fault caused between SAPO-34 and ZSM-5, which confirms the existence of a core-shell configuration of the S34@Z5 particle. The nanocrystallite morphology of the ZSM-5 shell layout of the particles bears the same orientation (Fig. 6A (iii), red rectangle). The same micro fault is observed even in the large space formed between the circular ZSM-5 and the corner of the cube-shaped SAPO-34, and the crystals on both sides of the cross-section show the same lattice crystalline orientations (Fig. 6A(iv)-(v)), implying that slight fusion and recrystallization at the interface between SAPO-34 and ZSM-5 could occur. Taken together, the binary zeolite composite with core-shell structures is constructed successfully via SAC.

Fig. 6B shows the NH_3-TPD results of the SAPO-34, ZSM-5, physical mixtures, and S34@Z5. A minor peak at 103 °C and a well-resolved peak at 335 °C are observed for ZSM-5, indicating that most acid sites are strong. Two distinctive desorption peaks are also detected for SAPO-34 at approximately 132 °C and 323 °C, respectively. The low-temperature desorption peak for SAPO-34 stems from external surface hydroxyl groups, and the high-temperature desorption peak assigned to strongly acidic sites are associated with Brønsted acid sites and Lewis acid sites [42]. The physical mixtures possess two discrete ammonia desorption broad peaks. For the S34@Z5 sample, the low-temperature desorption peak is almost absent. This could be ascribed to the transformation or neutralization of surface acid sites of SAPO-34 in the synthesis process of composite by the interface interactions between ZSM-5 and the SAPO-34, which is consistent with TEM characterization results.

Fig. 6C displays the N_2 physisorption isotherms at 77 K and pore size distributions for ZSM-5, SAPO-34, and S34@Z5. The initial parts of all of

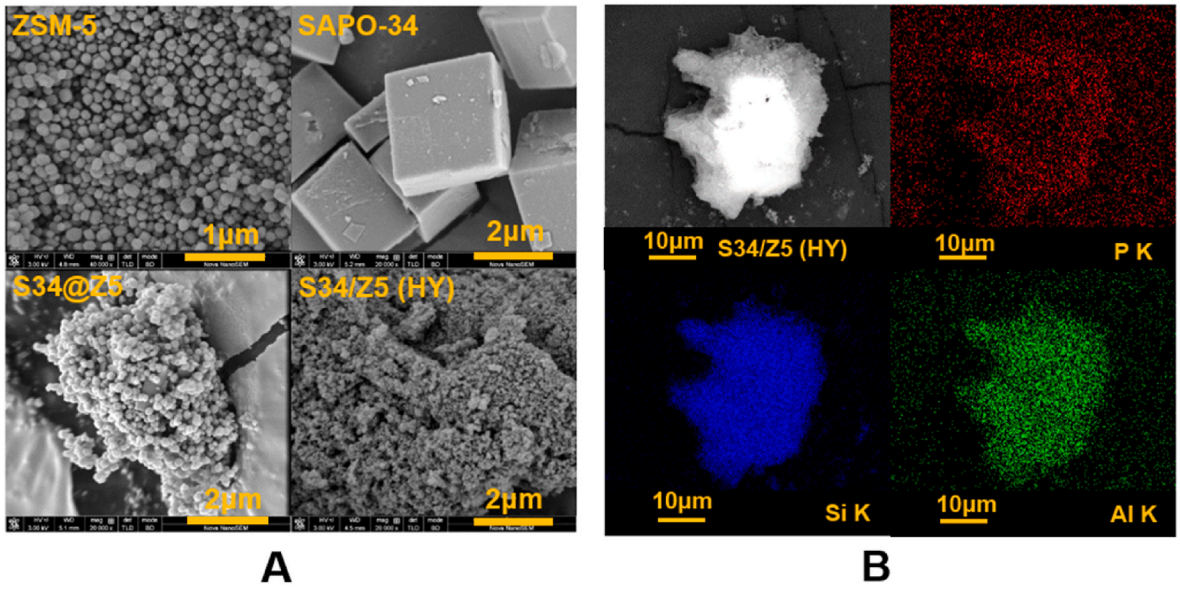

Fig. 5. A SEM images of the as-synthesized ZSM-5, SAPO-34, S34@Z5, and S34/Z5 (HY); B Elemental mapping (P, Al, and Si) of the S34/Z5 (HY).

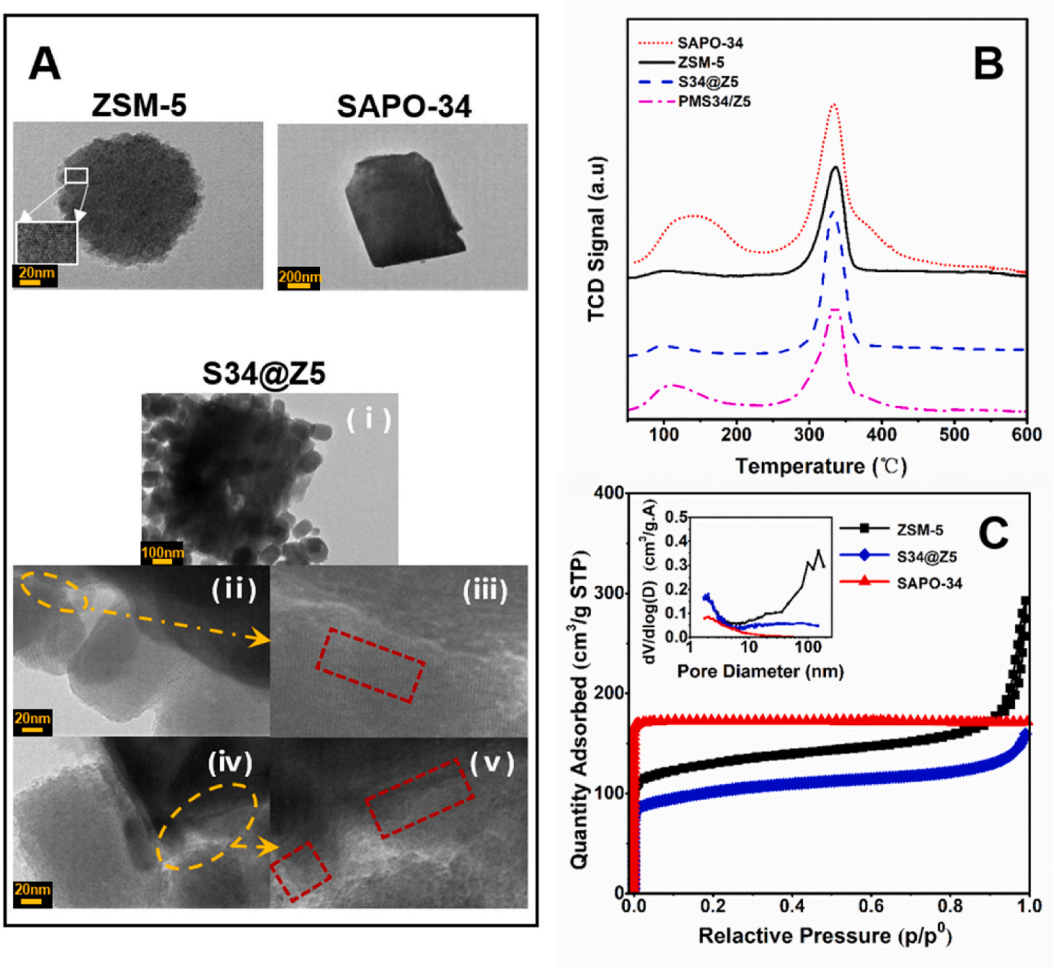

Fig. 6. A TEM images of the ZSM-5, SAPO-34 and S34@Z5. B NH3-TPD curves of SAPO-34, ZSM-5, S34@Z5 and PMS34/Z5 physical mixture. C N_2 adsorption-desorption isotherms and pore diameter distribution of ZSM-5, SAPO-34, and S34@Z5.

the samples exhibit a sharp slope of the isotherm at low relative pressures (P/P0 < 0.1), which can be ascribed to the characteristic micropore framework [43]. For the N_2 physisorption isotherm of ZSM-5, a sharp uptake in the high region of relative pressure ($P/P_0 > 0.95$) is discernible, which can be ascribed to the intercrystalline macropores of the packing particles. SAPO-34 shows a typical type I isotherm, illustrating the presence of high micropores. For the S34@Z5 zeolite, the slightly decreased micropores and absent stacking pores compared to those of ZSM-5 are obtained. The pore structure parameters of S34@Z5 were compared to that of the ZSM-5 sample in Table 1, an increased micropore proportion, and diminished BET surface area and total pore volume are observed.

Based on the XRD, SEM, EDS, HRTEM, NH_3-TPD and N_2 adsorption results above, the unique core-shell configuration of the S34@Z5 composite is obtained and compared to other samples to construct and allocate the filtering and catalytic functions of both ZSM-5 and SAPO-34.

3.2. Catalytic performance

The catalytic performances of all synthesized samples in the coupled conversion of *n*-hexane-methanol are investigated under the reaction condition of 580 °C, WHSV = 10 h^{-1}, N_2 = 30 mL/min, and methanol/n-hexane molar ratio = 1.6. As shown in Fig. 7A, the *n*-hexane conversion and product yield varied over diverse catalysts under the same reaction conditions. Methanol conversion was always higher than 98 wt%. For the single zeolite catalysts, SAPO-34 with a three-dimensional CHA structure exhibited a relatively high ethylene yield of 10.3 wt% and low *n*-hexane conversion of 26.4 wt%. The effective diameter of the *n*-hexane molecule is 0.49 nm; nevertheless, the pore mouth of the SAPO-34 is 0.38 × 0.38 nm and cannot allow *n*-hexane to enter its cage. MTO reaction occurred mainly in the SAPO-34 channel which was supported by the significantly lower C_2–C_4 alkanes yield (the yield of C_2–C_4 alkanes is 4.3 wt%). Compared with SAPO-34, ZSM-5 exhibited a high *n*-hexane conversion of 50.2 wt% because the MFI structure is incorporated by the interaction between a straight cylindrical channel with a diameter of 0.54 × 0.56 nm and a Z-channel with a diameter of 0.52 × 0.58 nm allows both reactants to enter at the same time. The higher butylene yield was obtained from the methanol-*n*-hexane co-reaction over ZSM-5, which inferred the alkene-based path was mainly followed in the coupling reaction system catalyzed by ZSM-5. The ethylene and propylene yields were altered by PMS34/Z5 as catalysts accompanied by the abatement of *n*-hexane conversion compared with that of ZSM-5. Accordingly, the *n*-hexane conversion is dependent on the ZSM-5 zeolite. In comparison of other samples, the performance of n-hexane-methanol co-reaction over S34@Z5 showed the highest *n*-hexane conversion and light olefin yield. A propylene yield of 27.2 wt% and an ethylene yield of 8.5 wt%, with an *n*-hexane conversion of 64.5 wt%, was obtained from S34@Z5. The difference in catalytic performance between S34@Z5 and PMS34/Z5 implies that the core-shell configuration of the composite could be a key factor in modulating the reaction routes and the degree of the coupling reaction between *n*-hexane and methanol for light olefins. The *n*-hexane conversion as a function of time on stream was depicted in Fig. 7B. SAPO-34 shows the shortest lifetime.

Table 1
Pore structure parameters of SAPO-34, ZSM-5, and S34@Z5 composite zeolites.

Samples	Surface area (m^2/g)			Pore volume (cm^3/g)	
	S_{BET}[a]	S_{mic}[b]	S_{ext}	V_t[c]	V_{mic}[b]
ZSM-5	420	302	118	0.39	0.15
S34@Z5	374	276	98	0.22	0.12
SAPO-34	578	553	25	0.27	0.25

[a] Obtained using the BET equation over a range of N_2 relative partial pressures P/P0 varying from 0.05 to 0.30.
[b] Calculated using the t-plot method.
[c] Calculated using the NLDFT method.

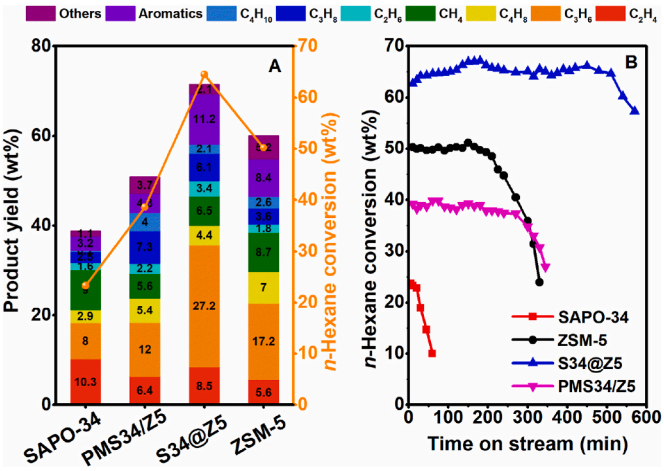

Fig. 7. A The yield of full products and n-hexane conversion for the SAPO-34, PMS34/Z5, S34@Z5 and ZSM-5 after the reactions become stable; B n-Hexane conversion as a function of time on stream for the SAPO-34, ZSM-5, S34@Z5 and PMS34/Z5. (Temperature = 580 °C, WHSV = 10 h^{-1}, N_2 = 30 mL/min and methanol/*n*-hexane molar ratio = 1.6. Aromatics: including BTX, ethylbenzene and tri-methylbenzene. Others: C_4^+ paraffins and olefins).

The PMS34/Z5 sample exhibited favorable stability of 270 min compared to that of ZSM-5 (210 min). The S34@Z5 composite had the highest catalytic lifespan of 510 min.

3.3. Carbonaceous deposits analysis

TG-DTG profiles in the airflow of spent zeolite samples after 1 h reaction are shown in Fig. 8. The sharp weight losses below 300 °C of all tested zeolites are ascribed to the desorption of the physical and chemical adsorbed moisture. The weight loss above 300 °C is associated with the oxidation of carbonaceous deposits in spent zeolites [44]. Based on TG-DTG profiles of spent zeolites, the fraction of carbonaceous deposits in different temperature ranges is summarized in Table 2.

As clearly illustrated in Table 2, the S34@Z5 core-shell zeolite exhibited the lowest carbonaceous deposit weight of 18 mg/$g_{catalyst}$, which could be the reason for its superior catalytic stability (Fig. 7B). The core-shell structure of composite zeolite minimizes carbon deposition by altering the diffusion path of the reactants and expanding the formation routes of the products (mainly in the SAPO-34 core layer). For instance, the ZSM-5 shell slows down the diffusion rate of methanol into the SAPO-34 core and avoids carbon deposition on the outer surface of SAPO-34, which can lengthen the diffusion trajectories of molecules. Similar carbonaceous deposit content was obtained from spent ZSM-5 and PMS34/Z5 for 30 mg/$g_{catalyst}$ and 27 mg/$g_{catalyst}$, respectively, even though, the distribution of carbonaceous species is significantly different with temperature. The carbonaceous deposits of the spent ZSM-5 sample mainly burn at a low-temperature range (300–500 °C). However, the weight loss caused by the combustion of carbonaceous deposits of spent PMS34/Z5 is mainly concentrated in 500–600 °C, which is similar to that of spent SAPO-34, inferring the carbonaceous species in the PMS34/Z5 physical mixture are mainly present in SAPO-34 pore. The carbonaceous deposits burning below 500 °C are related to more hydrogenated species, whereas the carbonaceous deposits burning above 500 °C to more carbonaceous ones [45]. SAPO-34 catalyst activity is null at 1 h time on stream, and it held the highest carbonaceous deposit content of 46 mg/$g_{catalyst}$. The carbonaceous deposits of spent SAPO-34 mainly burn above 500 °C.

It is well established in the literature that carbonaceous deposits originate from the condensation of reactive intermediates [46,47]. The distribution of carbonaceous deposits between spent ZSM-5 and spent SAPO-34 is significantly different, which is related to the different

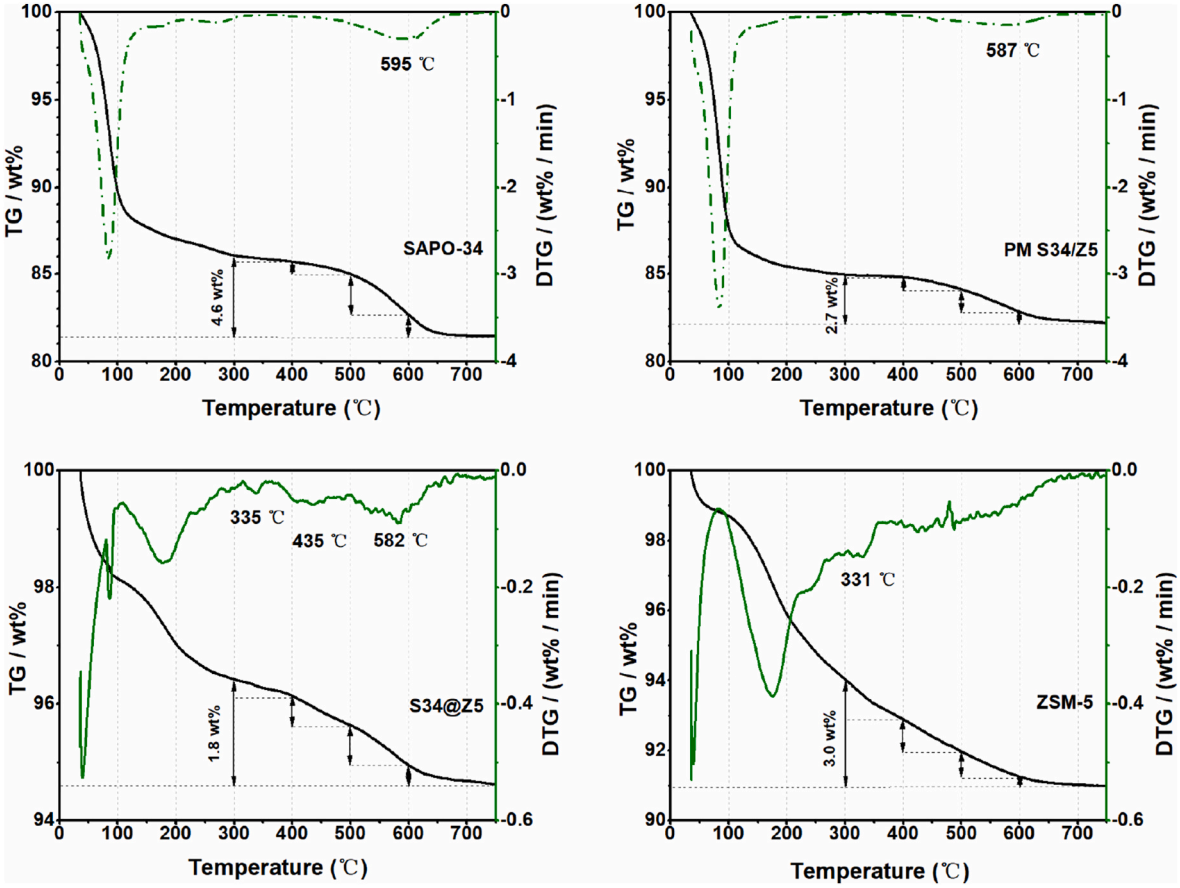

Fig. 8. TG-DTG profiles of spent catalysts obtained after n-hexane-methanol combined conversion at 580 °C for 1 h.

Table 2
The total amount of carbonaceous deposits on the spent zeolites after 1 h reaction determined by thermogravimetric analysis and fraction of carbonaceous deposits in different temperature ranges.

	Catalysts			
	SAPO-34	PMS34/Z5	S34@Z5	ZSM-5
Total amount of carbonaceous deposits (mg/$g_{catalyst}$)	46	27	18	30
Temperature range (°C)	Fraction of carbonaceous deposits (wt%)			
300-400	7.8	5.2	15.5	37.3
400-500	15.4	25.8	28.3	30.2
500-600	50.0	46.8	37.8	24.0
Over 600	26.8	22.2	18.4	8.5

product formation pathways caused by different skeletons.

The soluble organic species trapped in the spent SAPO-34 sample with different reaction times are detected by GC-MS, and the results are shown in Figure S1. Polymethylbenzenes, poly-methylcyclopentadiene, and long-chain alkanes are observed from the organic species trapped in the spent SAPO-34 sample at TOSs of 15 min and 580 °C. After a TOS of 1 h at 580 °C, PAHs including naphthalene, phenanthrene and pyrene as the predominant components over the SAPO-34 catalyst appeared accompanied by the diminishment of di-methylbenzene, poly-methylcyclopentadiene and lighter alkanes. These retained species suffering from a longer residence time were consumed via side reactions such as the π-interaction of cyclopentenyl cations with lighter aromatics, yielding PHAs and long-chain alkane species [47,48], which is consistent with the low lifespan of SAPO-34.

The GC/MS results for the extracted species in diverse samples at 1 h

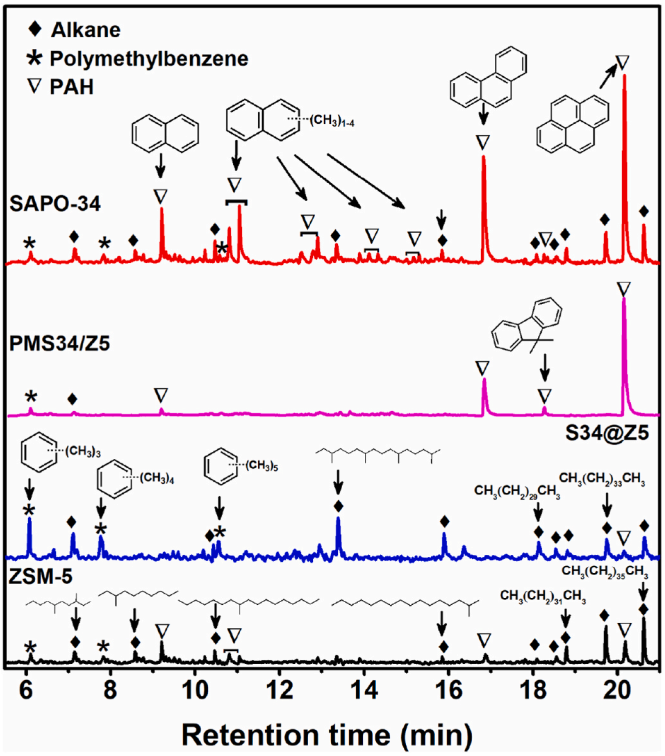

Fig. 9. GC-MS results for the extracted species in spent SAPO-34, PMS34/Z5, S34@Z5, and ZSM-5 at TOSs of 1 h and 580 °C.

of TOS and 580 °C are illustrated in Fig. 9. The extracted species in spent ZSM-5 are mainly long-chain alkanes and pyrene. According to the structural characteristics of ZSM-5, the pyrene is mainly from the external layer deposition [49]. Compared with the extracted species of spent ZSM-5, more phenanthrene and pyrene were obtained from that of spent SAPO-34, meanwhile, a series of new carbonaceous deposits poly-methyl naphthalene (including dimethyl naphthalene, tri-methyl naphthalene, and tetra-methyl naphthalene), which is coinciding with the deposition of more carbonaceous species in the SAPO-34 (Fig. 8). Pyrene and phenanthrene are identified as the dominant extracted species in PMS34/Z5. Compared with the extracted species of ZSM-5, reduced long-chain alkane and poly-methylnaphthalene are observed from the extracted species of PMS34/Z5. This could be related to the non-uniform distribution of methanol and *n*-hexane on PMS34/Z5 due to the skeletal differences between ZSM-5 and SAPO-34 [27]. There is no enhancement of poly-methylbenzene activity species from the extracted species of PMS34/Z5. As for the S34@Z5 composite, the concentration of polymethylbenzenes (involving tri-methylbenzene, tetra-methylbenzene, and penta-methylbenzene) as the active centers of the aromatic-based route is orders of magnitude higher than that found for other samples, suggesting the enhancement of the aromatic-based route [23]. A small amount of pyrene was obtained from the extracted species in S34@Z5 at TOSs of 1 h and 580 °C.

Combined with Fig. 7, the aromatics yield of co-reaction over diverse catalysts was in order: S34@Z5 11.2 wt% >ZSM-5 8.4 wt%>PM 4.3 wt %> SAPO-34 3.2 wt%. While the carbonaceous deposits on diverse catalysts were in order: SAPO-34 0.46 wt%>ZSM-5 0.3 wt%>PM 0.27 wt%>S34@Z5 0.18 wt%. For the SAPO-34 sample, the high amount of

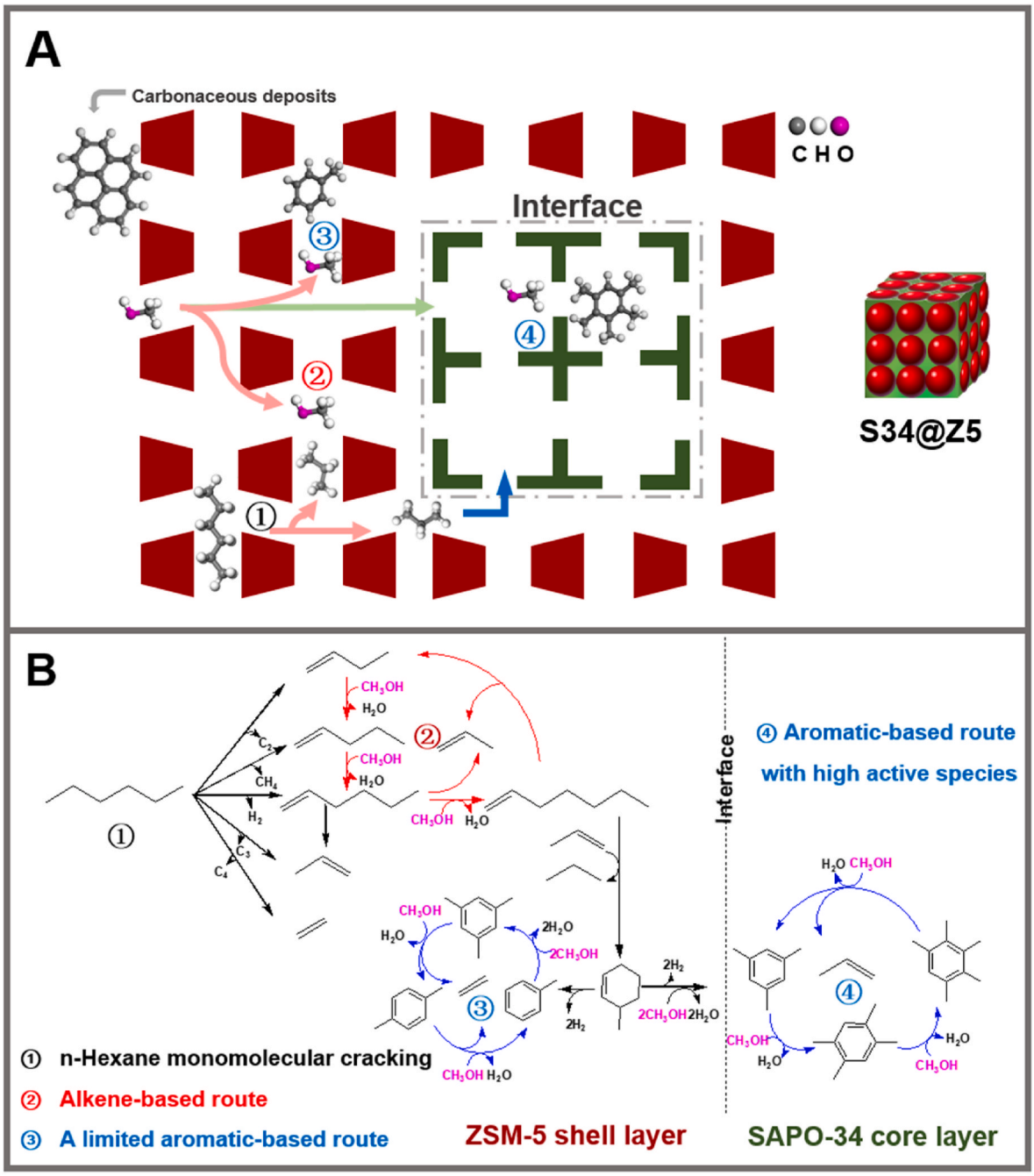

Fig. 10. A Possible diffusion trajectories of mixed feedstock and the location of carbonaceous deposits in S34@Z5 core-shell zeolite. B Proposed synergistic reaction path for the formation of light olefins from n-hexane-methanol on S34@Z5 core-shell zeolite.

carbonaceous deposits and low aromatics content indicated that the monocyclic aromatics (MAHs) cannot exist stably and were readily reacted with methanol to form polycyclic aromatic hydrocarbons (PHAs) in the SAPO-34 channel [11,48]. The S34@Z5 composite with core-shell structure displayed the highest yield of aromatics and the lowest amount of carbonaceous deposits. Based on the GC-MS analysis, the core-shell structure of S34@Z5 subdued the conversion of MAHs to PHAs, accordingly, more active intermediates of polymethylbenzenes were retained.

3.4. The synergistic reaction of N-hexane-methanol on S34@Z5

Compared with SAPO-34, the higher stability of HZSM-5 zeolite in the combined reaction of n-hexane-methanol is attributed to its porous structure without cages, which avoids the formation of heavy methylbenzene and PHAs in the pore channel. Accordingly, the carbonaceous deposits are mainly formed on the external surface of ZSM-5, which avoids blockage of the pore channel and reduction of active sites within the crystals. Whereas for SAPO-34 catalyst, the presence of cages favors the retention of heavy methylbenzenes (involving tetra-methylbenzene, penta-methylbenzene, and hexa-methylbenzene) that is the highly active species in the aromatics cycle route, meanwhile, easily causes the formation of PHAs in the cages. In addition, the formation of external coke in SAPO-34 is inevitable under high-temperature conditions. The deactivation of SAPO-34 was caused by external coke and carbonaceous deposits in the cage [50]. As for the S34@Z5 with core-shell structure, based on the analysis of the carbonaceous deposit by TG and GC/MS, the possible diffusion trajectories of mixed feedstock in S34@Z5 core-shell zeolite composite were illustrated in Fig. 10A. The diffusion rate of methanol towards the SAPO-34 core layer is slowed down due to its preferential adsorption on the ZSM-5 shell layer, and the short-chain hydrocarbon generated from *n*-hexane cracking enters the SAPO-34 cage through narrow pores providing a carbon source for the establishment of HCP in SAPO-34 cage. This could be a factor delaying the carbon deposition on the SAPO-34 cage of S34@Z5 [16]. In addition, the interfacial interaction between ZSM-5 and SAPO-34 resulted in the decrease of active sites on the external surface of the SAPO-34 core during the synthesis of S34@Z5 (Fig. 6), which avoids the external surface coking of SAPO-34 core. This reduces orifice blockage and preserves more active sites of the SAPO-34 core layer. High propylene selectivity in the SAPO-34 core layer depends on the abundant heavy methylbenzene, lower cage inside coking and reduced methanol diffusion rate in the SAPO-34 cage [16].

Based on the result of the carbonaceous deposit by TG and GC/MS, Fig. 10B schematizes the possible synergistic reaction path of *n*-hexane-methanol on S34@Z5. When co-reactions of *n*-hexane with methanol were carried out over S34@Z5, the preliminary cracking of *n*-hexane (*n*-hexane monomolecular cracking □) occurred in the ZSM-5 shell. Meanwhile, partial methanol was adsorbed on the ZSM-5 shell layer due to its high proton affinity [51]. Accordingly, the alkene-based route (red lines □) between alkenes derived from *n*-hexane catalytic/thermal cracking and methanol mainly took place on the ZSM-5 shell layer. A similar integration of the hydrocarbons catalytic cracking into the HCP route of methanol is also proposed by Cordero-Lanzac et al. [4]. The aromatic-based route (blue lines □) on the ZSM-5 shell layer was not significant due to the absence of highly active species [27,47]. However, the aromatic-based route (blue lines □) is the main reaction route over the SAPO-34 core layer with enough space for the accommodation of heavy methylbenzenes (involving tetra-methylbenzene, penta-methylbenzene, and hexa-methylbenzene) that have higher activity than low methylbenzene in the aromatic-based route.

The variation of the alkene-based route, however, cannot be visualized in GC-MS results. Combined with the catalytic performance of each catalyst, it should be noted that the enhancement of aromatic-based route and the improvement of catalytic performance in S34@Z5 can be ascribed to the enhanced synergistic effect of *n*-hexane/*n*-hexane derivatives with methanol, which is the result of the reasonable adjustment of reactants by the core-shell structure of composite.

4. Conclusions

In this work, the SAPO-34@ZSM-5 core-shell zeolite composite is designed and synthesized through the SAC method and used to enhance the synergies in the co-reaction of *n*-hexane and methanol to produce light olefins. The SAC method avoids the undesired phase transformation/dissolution of SAPO-34 caused by exposure to the strongly alkaline condition of the ZSM-5 precursor gel; accordingly, the well-defined SAPO-34@ZSM-5 composite is obtained. The reaction routes of *n*-hexane-methanol were reasonably regulated by the core-shell structure of SAPO-34@ZSM-5 to achieve a better synergistic effect. The increased propylene partly originates from the aromatic-based route in the SAPO-34 core layer. Moreover, the attenuation of methanol diffusion rate and the decreased outside surface active sites of SAPO-34, on account of the ZSM-5 shell layer, delayed the coking in the SAPO-34 cage. The optimum ratio of the two molecular sieves and the optimization of the reaction process (including replacing *n*-hexane with naphtha) are under intensive investigation.

CRediT authorship contribution statement

Qitong Cheng: Writing – original draft, Methodology, Data curation, Formal analysis, Visualization. **Benxian Shen:** Supervision, Resources. **Jichang Liu:** Writing – review & editing, Conceptualization, Supervision. **Hui Sun:** Writing – review & editing. **Di Wu:** Visualization. **Lei Jiang:** Investigation, Visualization. **Peikun Yan:** Visualization. **Xin Pu:** Visualization. **Suhui Ou:** Visualization. **Jigang Zhao:** Resources.

Declaration of competing interest

The authors declare that they have no known competing financial interests or personal relationships that could have appeared to influence the work reported in this paper.

Acknowledgment

The authors would like to acknowledge financial support from Joint Fund by the National Natural Science Foundation of China and Petro-China (Project U1862204).

The authors would like to thank the NS-TEST Co. for the characterization of catalysts.

Appendix A. Supplementary data

Supplementary data to this article can be found online at https://doi.org/10.1016/j.micromeso.2021.111298.

References

[1] R.L.V. Mao, A. Muntasar, H.T. Yan, Q. Zhao, Catalytic cracking of heavy olefins into propylene, ethylene and other light olefins, Catal. Lett. 130 (2009) 86–92.
[2] S.M. Sadrameli, Thermal/catalytic cracking of liquid hydrocarbons for the production of olefins: a state-of-the-art review II: catalytic cracking review, Fuel 173 (2016) 285–297.
[3] B. Lücke, A. Martin, H. Günschel, S. Nowak, CMHC: coupled methanol hydrocarbon cracking: formation of lower olefins from methanol and hydrocarbons over modified zeolites, Microporous Mesoporous Mater. 29 (1999) 145–157.
[4] T. Cordero-Lanzac, C. Martínez, A.T. Aguayo, P. Castaño, J. Bilbao, A. Corma, Activation of n-pentane while prolonging HZSM-5 catalyst lifetime during its combined reaction with methanol or dimethyl ether, Catal. Today (2020), https://doi.org/10.1016/j.cattod.2020.09.015.
[5] A. Kazemi, M. Beheshti, R. Khalili, Influence of recycle streams of C5/C6 and C4 hydrocarbon cuts on the performance of methanol to propylene (PVM) reactors, Chem. Eng. Sci. 172 (2017) 385–394.
[6] S.M. Yu, J.F. Wu, C. Liu, W. Liu, S. Bai, J. Huang, Alkane activation initiated by hydride transfer: Co-conversion of propane and methanol over H-ZSM-5 zeolite, Angew. Chem. 127 (2015).

[7] F. Chang, Y. Wei, X. Liu, Y. Zhao, L. Xu, Y. Sun, D. Zhang, Y. He, Z. Liu, A mechanistic investigation of the coupled reaction of n-hexane and methanol over HZSM-5, Appl. Catal. Gen. 328 (2007) 163–173.

[8] F. Chang, Y. Wei, X. Liu, Y. Qi, D. Zhang, Y. He, Z. Liu, An improved catalytic cracking of n-hexane via methanol coupling reaction over HZSM-5 zeolite catalysts, Catal. Lett. 106 (2006).

[9] W. Zhang, M. Zhang, S. Xu, S. Gao, Y. Wei, Z. Liu, Methylcyclopentenyl cations linking initial stage and highly efficient stage in methanol-to-hydrocarbon process, ACS Catal. 10 (2020) 4510–4516, https://doi.org/10.1021/acscatal.0c00799.

[10] E. Hernandez, F. Jentoft, Spectroscopic signatures reveal cyclopentenyl cation contributions in methanol-to-olefins catalysis, ACS Catal. 10 (2020) 5764–5782, https://doi.org/10.1021/acscatal.0c00721.

[11] W. Song, H. Fu, J.F. Haw, Selective synthesis of methylnaphthalenes in HSAPO-34 cages and their function as reaction centers in methanol-to-olefin catalysis, J. Phys. Chem. B 105 (2001) 12839–12843.

[12] W. Song, H. Fu, J. Haw, Supramolecular origins of product selectivity for methanol-to-olefin catalysis on HSAPO-34, J. Am. Chem. Soc. 123 (2001) 4749–4754.

[13] J.F. Haw, W. Song, D.M. Marcus, J.B. Nicholas, The mechanism of methanol to hydrocarbon catalysis, Acc. Chem. Res. 36 (2003) 317–326, https://doi.org/10.1002/chin.200330294.

[14] S. Ilias, R. Khare, A. Malek, A. Bhan, A descriptor for the relative propagation of the aromatic- and olefin-based cycles in methanol-to-hydrocarbons conversion on H-ZSM-5, J Journal of Catalysis 303 (2013) 135–140.

[15] S. Wang, Y. Chen, Z. Qin, T.-S. Zhao, S. Fan, M. Dong, J. Li, W. Fan, J. Wang, Origin and evolution of the initial hydrocarbon pool intermediates in the transition period for the conversion of methanol to olefins over H-ZSM-5 zeolite, J. Catal. 369 (2019) 382–395.

[16] J. Zhou, Y. Zhi, J. Zhang, Z. Liu, T. Zhang, Y. He, A. Zheng, M. Ye, Y. Wei, Z. Liu, Pre-situated "Coke"-Determined mechanistic route for ethene formation in methanol to olefins process on SAPO-34 catalyst, J. Catal. 377 (2019) 153–162.

[17] S.T. Sie, Acid-catalyzed cracking of paraffinic hydrocarbons. 1. Discussion of existing mechanisms and proposal of a new mechanism, Ind. Eng. Chem. Res. 31 (1992) 1881–1889.

[18] A. Corma, F.V. Melo, L. Sauvanaud, F. Ortega, Light cracked naphtha processing: controlling chemistry for maximum propylene production, Catal. Today 107–108 (2005) 699–706.

[19] S. Teketel, U. Olsbye, K.-P. Lillerud, P. Beato, S. Svelle, Selectivity control through fundamental mechanistic insight in the conversion of methanol to hydrocarbons over zeolites, Microporous Mesoporous Mater. 136 (2010) 33–41.

[20] H.T. Yan, R. Le Van Mao, Mixed naphtha/methanol feed used in the thermal catalytic/steam cracking (TCSC) process for the production of propylene and ethylene, Catal. Lett. 141 (2011) 691–698.

[21] D. Mier, A.T. Aguayo, A.G. Gayubo, M. Olazar, J. Bilbao, Synergies in the production of olefins by combined cracking of n-butane and methanol on a HZSM-5 zeolite catalyst, Chem. Eng. J. 160 (2010) 760–769.

[22] D. Mier, A.T. Aguayo, A.G. Gayubo, M. Olazar, J. Bilbao, Catalyst discrimination for olefin production by coupled methanol/n-butane cracking, Appl. Catal. Gen. 383 (2010) 202–210.

[23] M. Bjørgen, S. Svelle, F. Joensen, J. Nerlov, S. Kolboe, F. Bonino, L. Palumbo, S. Bordiga, U. Olsbye, Conversion of methanol to hydrocarbons over zeolite H-ZSM-5: on the origin of the olefinic species, J. Catal. 249 (2007) 195–207.

[24] S. Svelle, F. Joensen, J. Nerlov, U. Olsbye, K.-P. Lillerud, S. Kolboe, M. Bjørgen, Conversion of methanol into hydrocarbons over zeolite H-ZSM-5: ethene formation is mechanistically separated from the formation of higher alkenes, J. Am. Chem. Soc. 128 (2006) 14770–14771.

[25] M. Bjørgen, F. Joensen, K.-P. Lillerud, U. Olsbye, S. Svelle, The mechanisms of ethene and propene formation from methanol over high silica H-ZSM-5 and H-beta, Catal. Today 142 (2009) 90–97.

[26] B. Xu, C. Sievers, S.B. Hong, R. Prins, J.A. van Bokhoven, Catalytic activity of Brønsted acid sites in zeolites: intrinsic activity, rate-limiting step, and influence of the local structure of the acid sites, J. Catal. 244 (2006) 163–168.

[27] J. Li, Y. Wei, G. Liu, Y. Qi, P. Tian, B. Li, Y. He, Z. Liu, Comparative study of MTO conversion over SAPO-34, H-ZSM-5 and H-ZSM-22: correlating catalytic performance and reaction mechanism to zeolite topology, Catal. Today 171 (2011) 221–228.

[28] Q. Peng, G. Wang, Z. Wang, R. Jiang, D. Wang, J. Chen, J. Huang, Tuning hydrocarbon pool intermediates by the acidity of SAPO-34 catalysts for improving methanol-to-olefins reaction, ACS Sustain. Chem. Eng. 6 (2018) 16867–16875.

[29] S. Konnov, V. Pavlov, P. Kots, V. Zaytsev, I. Ivanova, Mechanism of SAPO-34 catalyst deactivation in the course of MTO conversion in slurry reactor, Catalysis Science & Technology 8 (2018) 1564–1577.

[30] L. Zhang, Z.-X. Jiang, Y. Yu, C.-S. Sun, Y.-J. Wang, H.-Y. Wang, Synthesis of core–shell ZSM-5@meso-SAPO-34 composite and its application in methanol to aromatics, RSC Adv. 5 (2015) 55825–55831.

[31] W. Jin, J. Ma, H. Ma, X. Li, Y. Wang, Hydrothermal synthesis of core-shell ZSM-5/SAPO-34 composite zeolites and catalytic performance in methanol-to-aromatics reaction, J. Solid State Chem. 267 (2018) 6–12.

[32] B. Mohammadkhani, M. Haghighi, E. Aghaei, Enhanced stability and propylene yield in methanol to light olefins conversion over nanostructured SAPO-34/ZSM-5 composite with various SAPO-loadings, Asia Pac. J. Chem. Eng. 14 (2019), e2274.

[33] H.-J. Chae, Y.-H. Song, K.-E. Jeong, C.-U. Kim, S.-Y. Jeong, Physicochemical characteristics of ZSM-5/SAPO-34 composite catalyst for MTO reaction, J. Phys. Chem. Solid. 71 (2010) 600–603.

[34] E. Moradiyan, R. Halladj, S. Askari, Beneficial use of ultrasound in rapid-synthesis of SAPO34/ZSM-5 nanocomposite and its catalytic performances on MTO reaction, Ind. Eng. Chem. Res. 57 (2018) 1871–1882.

[35] F. Magzoub, X. Li, S. Lawson, F. Rezaei, A.A. Rownaghi, 3D-printed HZSM-5 and 3D-HZM5@SAPO-34 structured monoliths with controlled acidity and porosity for conversion of methanol to dimethyl either, Fuel 280 (2020) 118628.

[36] Y. Li, Y. Wang, W. Qian, Z. Liu, L. Tang, L. Liang, C. Zhang, Q. Li, N. Xu, J. Sun, W. Shi, Achieving the super gas-wetting alteration by functionalized nano-silica for improving fluid flowing capacity in gas condensate reservoirs, ACS Appl. Mater. Interfaces 13 (2021).

[37] M. Razavian, S. Fatemi, Synthesis and application of ZSM-5/SAPO-34 and SAPO-34/ZSM-5 composite systems for propylene yield enhancement in propane dehydrogenation process, Microporous Mesoporous Mater. 201 (2015) 176–189.

[38] Z. Wang, C. Li, H.J. Cho, S.-C. Kung, M.A. Snyder, W. Fan, Direct, single-step synthesis of hierarchical zeolites without secondary templating, J. Mater. Chem. 3 (2015) 1298–1305.

[39] J. Zheng, D. Jin, Z. Liu, K. Zhu, X. Zhou, W. Yuan, Synthesis of nanosized SAPO-34 via an azeotrope evaporation and dry gel conversion route and its catalytic performance in chloromethane conversion, Ind. Eng. Chem. Res. 57 (2018) 548–558.

[40] Z. Deng, Y. Zhang, J. Zheng, K. Zhu, X. Zhou, A hierarchical bulky ZSM-5 zeolite synthesized via glycerol-mediated crystallization using a mesoporous steam-treated dry gel as the precursor, New J. Chem. 39 (2015) 7777–7780.

[41] J. Zheng, D. Jin, J. Ding, G. Ye, K. Zhu, X.-G. Zhou, W. Yang, W. Yuan, Tailored synthesis of nanosized SAPO-34 via time-controlled silicon release enabled by organosilane precursor, Chem. Commun. 53 (2017).

[42] L.-t. Kong, B.-x. Shen, J.-g. Zhao, J.-c. Liu, Comparative study on the chloromethane to olefins reaction over SAPO-34 and HZSM-22, Ind. Eng. Chem. Res. 53 (2014) 16324–16331.

[43] D. Serrano, J. Aguado, J. Escola, J. Rodriguez, A. Peral, Effect of the organic moiety nature on the synthesis of hierarchical ZSM-5 from silanized protozeolitic units, Journal of Materials Chemistry - J Mater Chem 18 (2008).

[44] D. Chen, K. Moljord, A. Holmen, A methanol to olefins review: diffusion, coke formation and deactivation on SAPO type catalysts, Microporous Mesoporous Mater. 164 (2012) 239–250.

[45] E. Epelde, M. Ibañez, A.T. Aguayo, A.G. Gayubo, J. Bilbao, P. Castaño, Differences among the deactivation pathway of HZSM-5 zeolite and SAPO-34 in the transformation of ethylene or 1-butene to propylene, Microporous Mesoporous Mater. 195 (2014) 284–293.

[46] M. Guisnet, P. Magnoux, Organic chemistry of coke formation, Appl. Catal. Gen. 212 (2001) 83–96.

[47] M. Guisnet, L. Costa, F.R. Ribeiro, Prevention of zeolite deactivation by coking, J. Mol. Catal. Chem. 305 (2009) 69–83.

[48] C. Wang, M. Hu, Y. Chu, X. Zhou, Q. Wang, G. Qi, S. Li, J. Xu, F. Deng, π-Interactions between cyclic carbocations and aromatics cause zeolite deactivation in methanol-to-hydrocarbon conversion, Angew. Chem. Int. Ed. 59 (2020) 7198–7202.

[49] T. Behrsing, H. Jaeger, J.V. Sanders, Coke deposits on H-ZSM-5 zeolite, Appl. Catal. 54 (1989) 289–302.

[50] J. Goetze, F. Meirer, I. Yarulina, J. Gascon, F. Kapteijn, J. Ruiz-Martínez, B. Weckhuysen, Insights into the activity and deactivation of the methanol-to-olefins process over different small-pore zeolites as studied with operando UV–vis spectroscopy, ACS Catal. 7 (2017) 4033–4046.

[51] J. Haw, Zeolite acid strength and reaction mechanisms in catalysis, ChemInform (2003) 34.